# Section 2

# Data sets, diagnostic and dynamical investigations, statistical post-processing , multi-year reanalyses and associated studies

# Climatology of satellite-derived cloud overlap parameter

Chernokulsky A.V., Eliseev A.V.
A.M. Obukhov Institute of Atmospheric Physics RAS
a.chernokulsky@ifaran.ru

Clouds are the main source of the uncertainties in modern global climate models (GCMs) [IPCC, 2007]. Different assumptions on cloud overlap implemented in a climate model may affect markedly modeled radiative fluxes [Barker et al., 1999]. Even small biases in fractional cloud cover can lead to substantial differences in climate feedbacks among global climate models [Clement et al., 2009].

For increasing the ability of climate models to simulate the real climate, it is preferable to know the value of the cloud overlap parameter α which is identified following by [Hogan and Illingworth, 2000]: $\alpha = (C_{true} - C_{rand})/(C_{max} - C_{rand})$, where $C_{true}$ is real cloud cover value, $C_{rand}$ is cloud cover obtained assuming random overlap and $C_{max}$ is cloud cover obtained assuming maximum overlap. Thus, α can treated as a measure of the relative weight of maximum (α = 1) and random (α = 0) overlap.

To estimate climatology of α we used quasi-simultaneous satellite observations from A-Train Aqua and CALIPSO satellites [Chernokulsky and Eliseev, 2012]. Values of $C_{true}$ were evaluated based on results of MODIS and CERES algorithms. Joint usage of CERES and MODIS data allow us to estimate the results' sensitivity to the initial data uncertainty. CALIPSO-GOCCP data were used to estimate cloud cover on different level and to compute values of $C_{rand}$ and $C_{max}$. Monthly means for 2006-2010 were used.

Cloud overlap parameter α derived from global annual means of $C_{true}$, $C_{rand}$ and $C_{max}$ is varied between 0.36 (for CERES $C_{true}$) and 0.26 (for MODIS $C_{true}$) (Table 1). It is smaller over the ocean and higher over land. This comes from prevailing random-overlapped stratiform clouds over the ocean and maximum-overlapped convective clouds over land. Thus, α may be used to diagnose relative contribution of convective and stratiform cloudiness to total cloud fraction. In general, annual cycle of α is larger over land than over the ocean (Fig. 1) because of convective processes activation over land during summer and increasing α. The most prominent annual cycle of α is noted in the monsoon regions where α is close to 1 in winter and almost 0 in summer.

Table 1. Values of α derived from global and hemispheric means of $C_{true}$, $C_{rand}$ and $C_{max}$. First value of α is based on CERES $C_{true}$, the second one is based on MODIS $C_{true}$.

| | | Annual | January | July |
|---|---|---|---|---|
| Global | Land+Ocean | 0.36 / 0.26 | 0.38 / 0.24 | 0.36 / 0.25 |
| | Only land | 0.49 / 0.40 | 0.51 / 0.37 | 0.48 / 0.40 |
| | Only ocean | 0.30 / 0.18 | 0.32 / 0.18 | 0.30 / 0.17 |
| Northern Hemisphere | Land+Ocean | 0.40 / 0.27 | 0.44 / 0.25 | 0.39 / 0.29 |
| | Only land | 0.50 / 0.40 | 0.58 / 0.36 | 0.46 / 0.40 |
| | Only ocean | 0.31 / 0.18 | 0.33 / 0.17 | 0.32 / 0.18 |
| Southern Hemisphere | Land+Ocean | 0.32 / 0.22 | 0.33 / 0.23 | 0.33 / 0.21 |
| | Only land | 0.47 / 0.40 | 0.38 / 0.37 | 0.54 / 0.40 |
| | Only ocean | 0.29 / 0.18 | 0.30 / 0.19 | 0.28 / 0.16 |

We found that α is linearly dependent on total cloud fraction in most regions, except in the southern tropics ocean. The maximum cloud overlap (α is close to 1) is associated with small values of cloud fraction and occurs in subtropical highs over the ocean and in subtropical and polar deserts over land (Fig. 2). On the other hand, the random cloud overlap (α is close to 0) occurs in regions with high values of cloud fraction (e.g. ITCZ and midlatitudinal storm

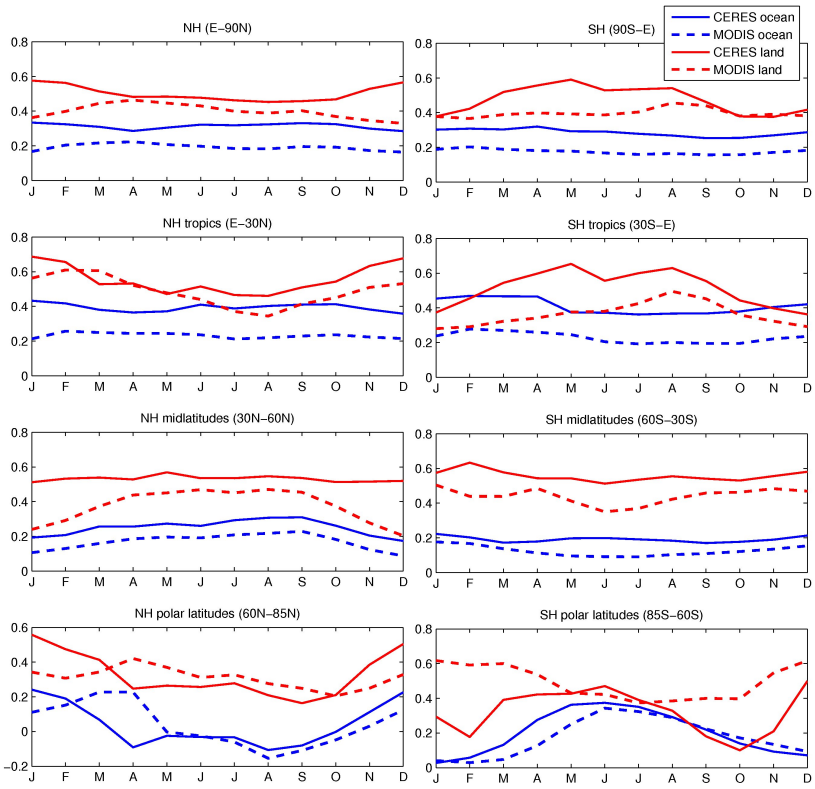


tracks) Moreover, we found that vast regions of the Southern Ocean (around 60S) are characterized by negative values of α, mostly in summer. Presumably, an assumption of the minimum overlap of cloud layers should be used in these regions due to strong baroclinic instability and horizontal shift of cloud layers.

Figure 1. Annual cycle of α for different regions.

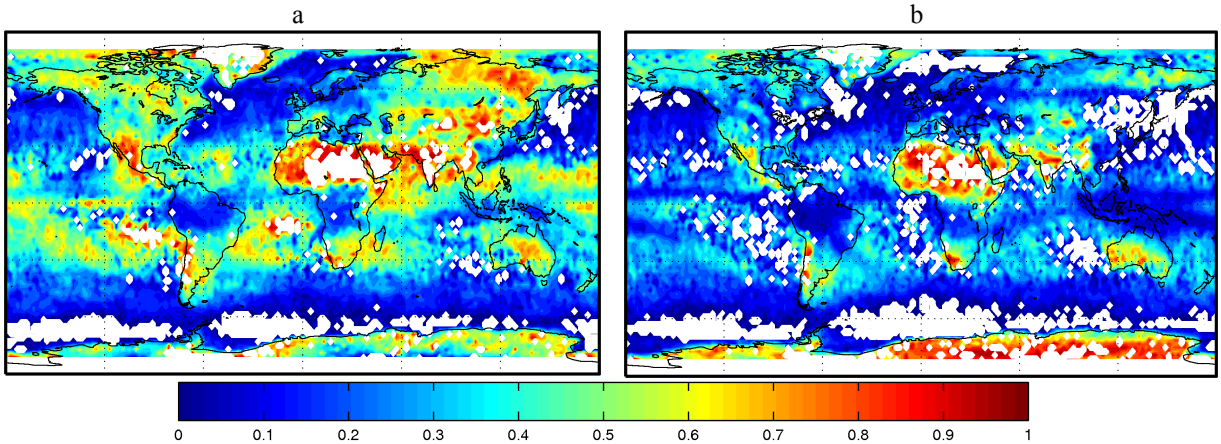


Figure 2. Climatology of α derived from annual means of $C_{rand}$, $C_{max}$ and $C_{true}$ (CERES (a) and MODIS (b)) (regions with α less than 0 and more than 1are blanked) .

**References**


1. Barker, H. W., G. L. Stephens, and Q. Fu. (1999). The sensitivity of domain-averaged solar fluxes to assumptions about cloud ge- ometry. *Quart. J. Roy. Meteor. Soc., 125*, 2127–2152.
2. Chernokulsky A.V. and Eliseev A.V. Assessing spatial distribution of cloud overlap parameter from satellite data. Abstracts of 3rd International Conference on Earth System Modelling. Hamburg, Germany. 2012. Abstract No 3ICESM-305.
3. Clement, A., Burgman, R., & Norris, J. R. (2009). Observational and Model Evidence for Positive Low-Level Cloud Feedback. *Science, 325* (5939), 460-464.
4. IPCC: The Physical Science Basis. Contribution of Working Group I to the Fourth Assessment Report of the Intergovernmental Panel on Climate Change *(Solomon S., Qin D., Manning M. et al., Eds.)*. Cambridge: Cambridge University Press, 2007. 996 pp.
5. Hogan, R. J., & Illingworth, A. J. (2000). Deriving cloud overlap statistics from radar. *Quart. J. Roy. Meteor. Soc.*, *126*, 2903–2909.

# A global ensemble reforecast data set for the 2012 NCEP Global Ensemble Forecast System

Thomas M. Hamill, Gary T. Bates, Jeffrey S. Whitaker, Donald R. Murray, Michael Fiorino, Thomas J. Galarneau, Jr.

NOAA Earth System Research Lab, Boulder, Colorado USA
Contact: Tom.Hamill@noaa.gov

A multi-decadal ensemble reforecast database is now available that is approximately consistent with the operational 00 UTC cycle of the 2012 NOAA Global Ensemble Forecast System (GEFS). The reforecast data set consists of an 11-member ensemble run once each day from 0000 UTC initial conditions. Reforecasts are run to +16 days. As with the operational 2012 GEFS, the reforecast is run at T254L42 resolution (approximately ½-degree grid spacing, 42 levels) for week +1 forecasts and T190L42 (approximately ¾-degree grid spacing) for the week +2 forecasts. Reforecasts were initialized with Climate Forecast System Reanalysis initial conditions, and perturbations were generated using the ensemble transform with rescaling technique. Reforecast data are available from 1985 to current.

Reforecast data sets were previously demonstrated to be very valuable for detecting and correcting systematic errors in forecasts, especially forecasts of relatively rare events and longer-lead forecasts. What is novel about this reforecast data set relative to the first-generation NOAA reforecast is that: (a) a modern, currently operational version of the forecast model is used (the previous reforecast used a model version from 1998); (b) a much larger set of output data have been saved, including variables relevant for precipitation, hydrologic, wind-energy, solar-energy, severe weather, and tropical cyclone forecasting; and (c) the archived data are at much higher resolution.

For a lengthier description of the reforecast configuration and some examples of how these second-generation reforecast data may be used for research and a variety of weather forecast applications, please see the upcoming BAMS article, at
http://www.esrl.noaa.gov/psd/people/tom.hamill/reforecastv2_bams_rev3.pdf

# EXTRATROPICAL TRANSITION OF TROPICAL CYCLONES: TENDECIES OF CHANGE

Mokhov I.I.[1], Dobryshman E.M.[1], M.E. Makarova[2]

[1] *A.M. Obukhov Institute of Atmospheric Physics RAS, Moscow*
[2] *Hydrometeorological Centre of Russia, Moscow*
mokhov@ifaran.ru

Significant part of tropical cyclones transform into extratropical cyclones (Jones et al., 2003; Klein et al., 2000). Tendencies of change for characteristics of extratropical transition (ET) for different oceanic basins in the Northern (NH) and Southern (SH) Hemispheres on the basis of observations for the period 1970-2012 are analyzed.

Table 1 shows annual-mean numbers of tropical cyclones $N_{tc}$ , tropical cyclones transformed into extratropical cyclones $N_{etc}$ and their relationship $N_{etc}/N_{tc}$ from observations during 1970-2012 for different basins: Western North Pacific (WNP), North Atlantic (NA), Eastern North Pacific (ENP), Northern Indian Ocean (NIO), Southern Indian Ocean (SIO), Southern Pacific (SP) and also for the globe, NH and SH as a whole.

Table 1. Annual-mean numbers of tropical cyclones $N_{tc}$ , tropical cyclones transformed into extratropical cyclones $N_{etc}$ and their relationship $N_{etc}/N_{tc}$ for different basins with hemispheric (NH, SH) and global means from observations for the period 1970-2012.

| Basin | | Tropical cyclones annual-mean number $N_{tc}$ | Tropical cyclones transformed into extratropical cyclones annual-mean number $N_{etc}$ | $N_{etc}/N_{tc}$ |
|---|---|---|---|---|
| NH | WNP | 25.3 | 8.9 | 0.35 |
| | NA | 11.1 | 4.5 | 0.41 |
| | ENP | 15.4 | 0.2 | 0.02 |
| | NIO | 4.9 | 0 | 0 |
| NH | | 56.7 | 13.7 | 0.24 |
| SH | SIO | 15.8 | 4.9 | 0.31 |
| | SP | 9.0 | 4.3 | 0.48 |
| SH | | 24.8 | 9.2 | 0.37 |
| Global | | 81.5 | 22.9 | 0.28 |

The largest ET frequency about 9 events per year is in the WNP basin. The appropriate events in the NA, SIO and SP basins are significantly more rare (less than 5 events per year).

Table 2 shows annual-mean values of $N_{tc}$, $N_{etc}$ and $N_{etc}/N_{tc}$ in the WNP basin for different decades. According to Table 2 there is a general inter-decadal decrease of $N_{tc}$ in the WNP basin with an appropriate general increase of $N_{etc}$ . As a result the ET probability in the WNP was in the first decade of the 21st century about 50%.

Table 2. Annual-mean numbers of tropical cyclones $N_{tc}$ , tropical cyclones transformed into extratropical cyclones $N_{etc}$ and their relation $N_{etc}/N_{tc}$ f in the WNP basin for different decades.

| WNP | $N_{tc}$ | $N_{etc}$ | $N_{etc}/N_{tc}$ |
|---|---|---|---|
| 1970-1979 | 26.6 | 8.1 | 0.30 |
| 1980-1989 | 26.6 | 6.7 | 0.25 |
| 1990-1999 | 25.8 | 9.6 | 0.37 |
| 2000-2009 | 23.6 | 11.6 | 0.49 |

Table 3 shows annual-mean values of $N_{tc}$, $N_{etc}$ and $N_{etc}/N_{tc}$ in the NA basin for different decades. According to Table 3 there is a general inter-decadal increase of $N_{tc}$ in the NA basin with a general increase of $N_{etc}$ during last decades.

Table 3. Annual-mean numbers of tropical cyclones $N_{tc}$, tropical cyclones transformed into extratropical cyclones $N_{etc}$ and their relation $N_{etc}/N_{tc}$ f in the NA basin for different decades.

| NA | $N_{tc}$ | $N_{etc}$ | $N_{etc}/N_{tc}$ |
|---|---|---|---|
| 1970-1979 | 8.1 | 4.0 | 0.49 |
| 1980-1989 | 8.6 | 2.8 | 0.33 |
| 1990-1999 | 10.5 | 4.2 | 0.40 |
| 2000-2009 | 14.8 | 5.7 | 0.39 |

Statistically significant positive trends for the number of extratropical cyclones ($N_{etc}$) transformed from tropical ones ($N_{tc}$) were obtained for the NH and for the globe as a whole with the largest trends for the WNP and NA basins (about 0.8 per decade). Statistically significant trends are obtained also for the part of tropical cyclones transformed into extratropical ones ($N_{etc}/N_{tc}$) for the NH (about 4% per decade) and for the globe as a whole (more than 3% per decade) with the largest trend for the WNP basin (more than 5% per decade). At the same time no statistically significant trend was found for $N_{etc}/N_{tc}$ in the NA basin.

Analysis of relationships of the ET characteristics with temperature changes during last decades shows positive correlation of $N_{etc}/N_{tc}$ for the NH and WNP basin with surface temperature changes in tropical latitudes. There is also negative correlation of the ET probability in the NH with temperature difference between tropics and extratropics. Significant coherency was obtained for the ET events in the WNP basin with El-Nino conditions.

**References**

Jones S.C., Harr P.A., Abraham J. et al., 2003: The extratropical transition of tropical cyclones: Forecast challenges, current understanding, and future directions. *Weather and Forecasting,* **18**, 1052-1092.

Klein P.M., Harr P.A., Elsberry R.L., 2000: Extratropical transition of Western North Pacific tropical cyclones: An overview and conceptual model of the transformation stage. *Weather and Forecasting*, **15**, 373-395.

# MESOPAUSE TEMPERATURE VARIATIONS UNDER GLOBAL CLIMATE CHANGES FROM OBSERVATIONS DURING LAST 5 DECADES

Mokhov I.I., Semenov A.I.

*A.M. Obukhov Institute of Atmospheric Physics RAS, Moscow*
mokhov@ifaran.ru

Detection of global climate changes from observations at the surface and in the low atmosphere (troposphere) should be accompanied by observations in the middle and upper atmosphere (Beig et al., 2003). Here, variations of temperature ($T_m$) at the mesopause from measurements during 1960-2012 at the Zvenigorod Scientific Station (56N, 37E) of the A.M. Obukhov Institute of Atmospheric Physics (ZSS IAP RAS) (Semenov et al., 2002) are analyzed in comparison with the global climate changes. Global climate changes during last decades are characterized by a global surface air temperature anomalies (relative to the 1961-1990 conditions) $T_{gs}$ (http://www.cru.uea.ac.uk/cru/data/temperature/).

Dataset for Tm (at 87 km) at the ZSS IAP RAS is the longest one in the global NDMC (Network for the Detection of Mesopause Change, http://wdc.dlr.de/ndmc/) system. These data are obtained by measurements on the hydroxyl rotational temperature records at the ZSS since 1957 (Golitsyn et al, 1996).

Interannual variations on Fig. 1 show strong general $T_m$ decrease during last half a century from observations in winter (December-January-February) at the ZSS IAP RAS with a significant slowing of this cooling during last 3 decades. Total range of $T_m$ variations for last 53 winters is 35K (from 242K to 207K). Mean linear trend $dT_m/dt$ for this period equals to -0.7 K/yr (with coefficient of correlation $r$=0.93).

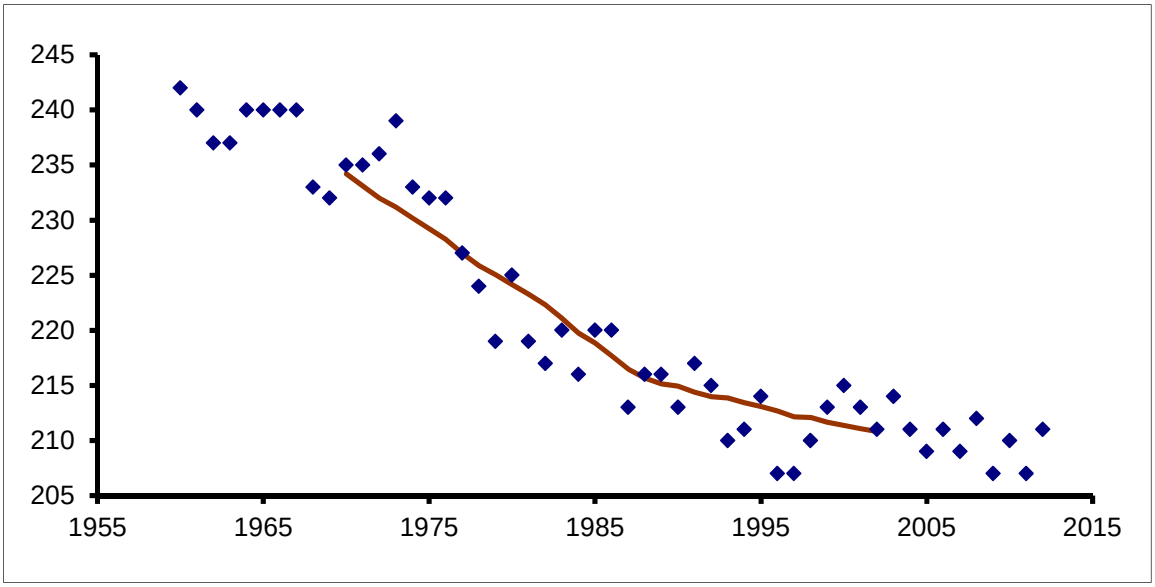


Fig. 1. Interannual $T_m$ variations (K) from observations in winter at the ZSS IAP RAS during the period 1960-2012 (bold line - smoothed with 21-year averaging).

Smoothed $T_m$ variations on Fig. 1 display quite clear decrease in the slope of the bold line after 1987. Linear trend of $T_m$ for the first 27 years (1960-1986) is equal to -1.0 K/yr ($r$=0.92), while for the second 26 years (1987-2012) $dT_m/dt$=-0.24 K/yr ($r$=0.58) – more than 4 times less. It should be noted abrupt $T_m$ decrease on 13K during 3 years from 1976 to 1979 (on 5K, 3K and 5K for 1976-1977, 1977-1978 and 1978-1979 transitions, respectively). For the first 17 years of analyzed dataset (1960-1976) before the abrupt $T_m$ decrease the linear trend equals to -0.49 K/yr

($r$=0.72), for the period 1978-1994 $dT_m/dt$ equals to -0.67 K/yr ($r$=0.82), but for the last 17 years (1996-2012) it is one order less (-0.07 K/yr) and statistically insignificant ( $r$=0.13).

The abrupt $T_m$ decrease between 1976 and 1979 with a transition to new conditions since 1980s is quite clear from Fig. 2 for dependence of $T_m$ variations at the ZSS IAP RAS on $T_{gs}$ anomalies during 1960-2012. According Fig. 2 there is a significant general $T_m$ decrease accompanying the general $T_{gs}$ increase during last decades. Relative changes of $T_m$ and $T_{gs}$ can be assessed from corresponding linear regression: $dT_m/dT_{gs}$= -35.0 ($r$=0.75) for the total period 1960-2012. For the first 27 years (1960-1986) the value of $dT_m/dT_{gs}$ was assessed to be equal to -21.0 ($r$=0.43), while for the second 26 years (1987-2012) $dT_m/dT_{gs}$ =-3.2 ($r$=0.17) – almost 7 times less (and less significant). For the first 17 years of analyzed dataset (1960-1976) before the abrupt $T_m$ decrease the $dT_m/dT_{gs}$ value was assessed to be equal to 7.2 ($r$=0.33), for the period 1978-1994 it equals to -5.5 ($r$=0.17), and for the last 17 years (1996-2012) it was estimated to be equal to 2.8 ( $r$=0.16).

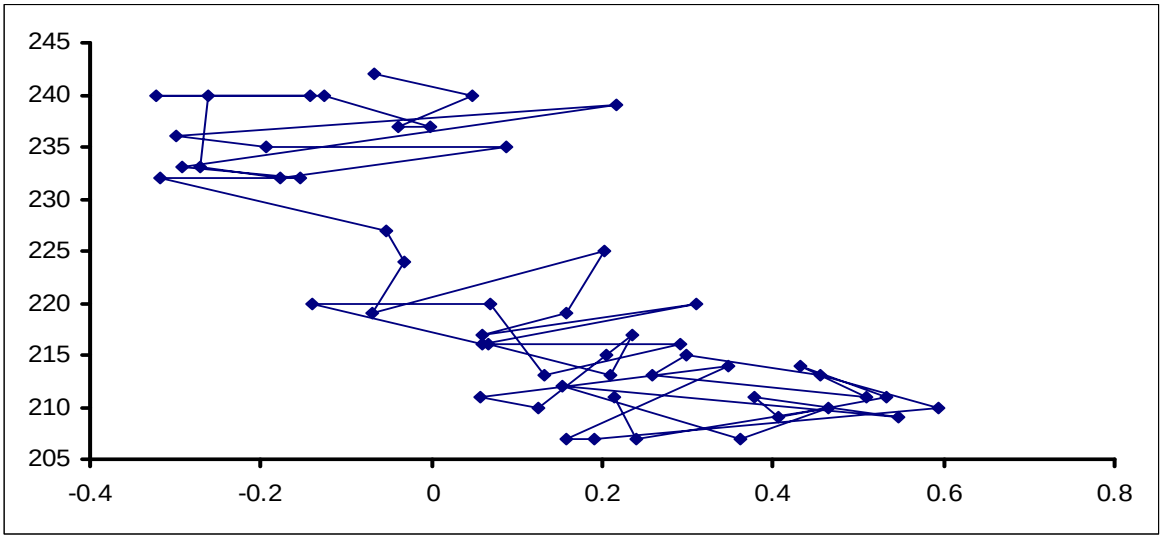


Fig. 2. Dependence of $T_m$ variations (K) at the ZSS IAP RAS on $T_{gs}$ anomalies (K) in winter (DJF) during 1960-2012.

The most significant relationship for $T_m$ with $T_{gs}$ was obtained for the total analyzed time interval (1960-2012). For shorter analyzed intervals such relationship is less significant and there are essential differences for various decadal-scale intervals. Cross-wavelet analysis exhibits significant differences in local coherence between $T_m$ and $T_{gs}$ for interannual and decadal variations and for various time intervals. Results of similar analysis of long-term model simulations show long-term negative coherence of $T_m$ and $T_{gs}$ variations with periods larger than 3 decades. To display such a coherence from observations it is necessary to have twice longer data set for $T_m$.

## References

Beig G., P. Keckhut, R.P. Lowe et al., 2003: Review of mesospheric temperature trends. *Rev. Geophys.*, **41**(4), 1015, doi:10.1029/2002RG000121.

Golitsyn G.S., A.I. Semenov, N.N. Shefov et al., 1996: Long-term temperature trends in the middle and upper atmosphere. *Geophys. Res. Lett.*, **23**, 1741-1744.

Semenov A.I., N.N. Shefov, E.N. Lysenko et al., 2002: The season peculiarities of behavior of the long-term temperature trends in the middle atmosphere on the mid-latitudes. *Phys. Chem. Earth*, **27**, 529-534.

# SPRING-SUMMER CLIMATE ANOMALIES IN EUROPEAN RUSSIA: ASSESSMENT OF ENSO EFFECTS

I.I. Mokhov, A.V. Timazhev

A.M. Obukhov Institute of Atmospheric Physics RAS, Moscow, Russia
mokhov@ifaran.ru, timazhev@gmail.com

Probabilities of climate anomalies in the Eurasian regions by observations from the end of 19th century to the beginning of the 21st century with an assessment of ENSO effects are studied (Mokhov, 2005; Mokhov, 2011; Mokhov et al., 2013). In particular, anomalies of surface air temperature, precipitation and drought index during May-July (growing season) in mid-latitudes for the European (ER) and Asian parts of Russia by data from (Mesherskaya and Blazhevich, 1997; Meshcherskaya et al., 2011) for the period 1891-2010 are analyzed.

Table 1 shows estimates of probabilities for temperature anomalies in the ER during May-July in different ENSO phases change during 1891-2010 (n – number of years for different ENSO phases). There are probabilities for positive and negative temperature anomalies and also for large (±1K) positive and negative temperature anomalies. Positive temperature anomalies and large positive anomalies in May-July are more frequent for ER for years starting with El Niño (E) events and the most frequent for transition to the years starting with La Niña (L) events (E→L). The E→L transition is characterized also by the lowest probability for negative temperature anomalies. The biggest probability of large negative temperature anomalies was obtained for the L→E transition and also for the N→E transition.

Table 1. Probabilities of the May-July temperature anomalies in ER for different ENSO phases during 1891-2010.

| Temperature anomaly probability | Year starts with neutral phase of ENSO | | | Year starts with El Niño | | | Year starts with La Niña | | |
|---|---|---|---|---|---|---|---|---|---|
| | *N→E (n=17)* | *N→L (n=11)* | *N→N (n=37)* | *E→E (n=3)* | *E→L (n=9)* | *E→N (n=15)* | *L→E (n=7)* | *L→L (n=9)* | *L→N (n=12)* |
| >0 | 0.47 | 0.64 | 0.57 | 0.67 | 0.89 | 0.47 | 0.29 | 0.33 | 0.17 |
| | 0.52 | | | 0.63 | | | 0.25 | | |
| >1K | 0.06 | 0.18 | 0.22 | 0 | 0.56 | 0.13 | 0.29 | 0.11 | 0 |
| | 0.17 | | | 0.26 | | | 0.11 | | |
| <0 | 0.47 | 0.36 | 0.35 | 0.33 | 0.11 | 0.53 | 0.57 | 0.56 | 0.58 |
| | 0.38 | | | 0.37 | | | 0.57 | | |
| ≤-1K | 0.24 | 0.18 | 0.11 | 0 | 0 | 0.20 | 0.29 | 0 | 0.08 |
| | 0.15 | | | 0.11 | | | 0.11 | | |

Table 2 shows estimates of probabilities for positive and negative precipitation anomalies in the ER during May-July in different ENSO phases change during 1891-2010. The most significant positive difference between probabilities for positive and negative precipitation anomalies are for years starting with El Nino, in particular for E→L and E→E transitions and also for L→N transition. These transitions are characterized by the most frequent positive precipitation anomalies and by the lowest probabilities for negative precipitation anomalies. The biggest probabilities of negative precipitation anomalies were obtained for the L→E and N→N transitions.

Table 2. Probabilities of the May-July precipitation anomalies in ER for different ENSO phases during 1891-2010.

| Precipitation anomaly probability | Year starts with neutral phase of ENSO | | | Year starts with El Niño | | | Year starts with La Niña | | |
|---|---|---|---|---|---|---|---|---|---|
| | *N→E (n=17)* | *N→L (n=11)* | *N→N (n=37)* | *E→E (n=3)* | *E→L (n=9)* | *E→N (n=15)* | *L→E (n=7)* | *L→L (n=9)* | *L→N (n=12)* |
| >0 | 0.58 | 0.55 | 0.46 | 0.67 | 0.67 | 0.60 | 0.43 | 0.56 | 0.67 |
| | 0.49 | | | 0.63 | | | 0.57 | | |
| <0 | 0.47 | 0.45 | 0.54 | 0.33 | 0.33 | 0.40 | 0.57 | 0.44 | 0.33 |
| | 0.51 | | | 0.37 | | | 0.43 | | |

Table 3 shows estimates of droughts probabilities in the ER during May-July in different ENSO phases change during 1891-2010. There are probabilities conditions with drought index larger (or equal) 10%, 20% and 30%. The largest probability of drought conditions of different intensity was obtained for the E→L transition.

Table 3. Drought index probability for different cases of ENSO phases change for May-July from observations (1891-2010).

| Drought index probability | Year starts with neutral phase of ENSO | | | Year starts with El Niño | | | Year starts with La Niña | | |
|---|---|---|---|---|---|---|---|---|---|
| | *N→E (n=17)* | *N→L (n=11)* | *N→N (n=37)* | *E→E (n=3)* | *E→L (n=9)* | *E→N (n=15)* | *L→E (n=7)* | *L→L (n=9)* | *L→N (n=12)* |
| ≥10% | 0.47 | 0.55 | 0.76 | 0.67 | 1 | 0.53 | 0.57 | 0.56 | 0.67 |
| | 0.65 | | | 0.70 | | | 0.61 | | |
| ≥20% | 0.35 | 0.45 | 0.57 | 0.33 | 0.78 | 0.33 | 0.29 | 0.22 | 0.25 |
| | 0.49 | | | 0.48 | | | 0.25 | | |
| ≥30% | 0.12 | 0.27 | 0.24 | 0 | 0.44 | 0.13 | 0.29 | 0.22 | 0.08 |
| | 0.22 | | | 0.22 | | | 0.18 | | |

According to obtained results the largest frequency of conditions with hot temperature and drought during May-July in ER is characteristic for the E→L transition. Such conditions were realized for European part of Russia in summer 2010.

## References


Meshcherskaya A.V., and V.G. Blazhevich, 1997: The drought and excessive moisture indices in a historical perspective in the principal grain-producing regions of the Former Soviet Union. *J. Climate*, **10**, 2670-2682.

Meshcherskaya A.V., M.P. Golod and V.M. Mirvis, 2011: The drought in 2010 against the background of multiannual changes in aridity in the major grain producing regions of the European part of Russia. *Proc. MGO*, 563, 1-27. (in Russian)

Mokhov I.I., 2005: Spring-summer climate extremes in Eurasian midlatitudinal regions. *Research Activities in Atmospheric and Oceanic Modelling*. J. Cote (ed). Geneva: WCRP, WMO TD-No.1276, S.02, 07–08.

Mokhov I.I., 2011: Specific features of the 2010 summer heat formation in the European territory of Russia in the context of general climate changes and climate anomalies. *Izvestiya, Atmos. Oceanic Phys.,* **47**(6), 653-660.

Mokhov I.I., M.G. Akperov, M.A. Prokofyeva, A.V. Timazhev, A.R. Lupo and H. Le Treut, 2013: Blockings in the Northern Hemisphere and Euro-Atlantic region: Estimates of changes from reanalysis data and model simulations. *Doklady Earth Sci.,* **449**(2), 430-433.

**Potential sources of aerosol pollution of the Moscow region**

K.A. Shukurov

*A.M. Obukhov Institute of atmospheric physics RAS, Moscow, Russia*

*karim.shukurov@ifaran.ru*

In 2011-2012 regular measurements of PM1.0, PM2.5, PM5.0 and PM10 were carried out at the Zvenigorod Scientific Station (ZSS) of A.M. Obukhov Institute of atmospheric physics RAS using Russian photoelectric particle counter AZ-10-03. In the period there were 298 measurements of the mass concentration of aerosol in all seasons and at different air masses and meteorological conditions. The measurements were conducted at 10:00 UTS at minimal relative air humidity and therefore when aerosol particles are dry maximally. For analysis of potential sources of aerosols PM1.0 was used as it consists of small (less then 1 mcm) aerosol particles that can fly in atmosphere for a longer time (several days) and can be transported for a longer distances than particles of fractions PM2.5-PM1.0.

Using the trajectory model HYSPLIT [1,2] ensemble of 5-days backward trajectories of air masses was calculated for the heights 10 m and 200 m above ground level for all days of measurements. Using special software the distributions of probability of backward trajectories were mapped for the two different types of aerosol weather at ZSS: a) when local minimal values of PM1.0 were observed (Fig.1a) and b) when local maximum values of PM1.0 were observed (Fig.1b).

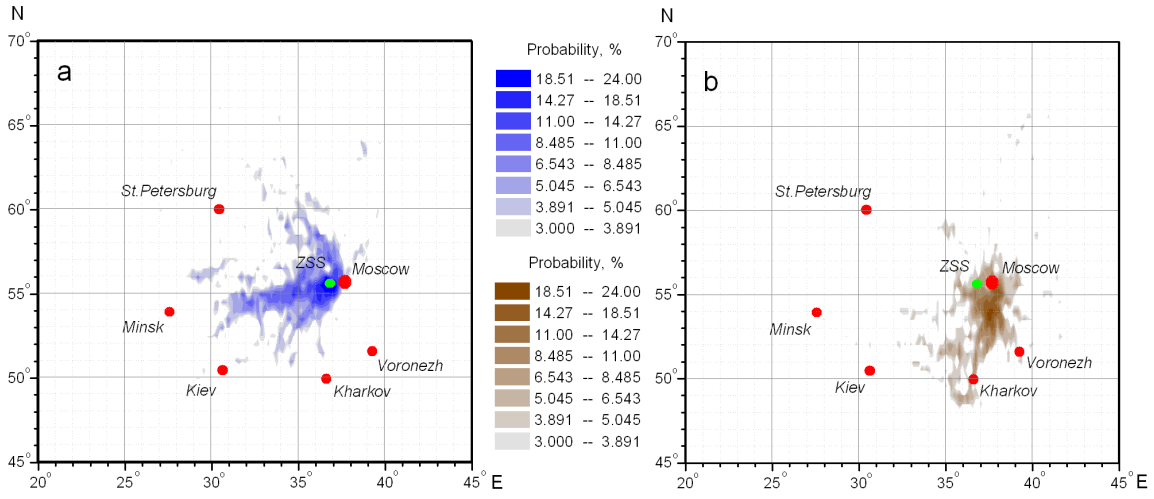


Figure 1. Spatial distribution of the probabilities of 5-day backward trajectories for ZSS calculated for a) events of local minima of aerosol upload at ZSS, b) events of local maxima of aerosol upload at ZSS.

As it seen from Fig.1 the regions of localization of the backward trajectories related to the local aerosol minima as well as to the local aerosol maxima: a) are distributed asymmetrically in wide space around the ZSS and b) practically are not superposed if probability of backward trajectory is above 9-11%. Some superposition of the regions at low probabilities of backward trajectories may be caused by: a) variation of local aerosol maxima in wide range of concentration and b) relatively short datasets of local aerosol maxima and local aerosol

minima used for the analysis. Moreover the superposition may be caused by potential seasonal variation of localization of trajectories of air masses with high aerosol upload.

Nevertheless the dividing of the regions of backward trajectories of air masses with and without high aerosol upload may give opportunity to reveal the region polluting with aerosols the Moscow region. As it seen from Fig.1b the region of potential aerosol sources polluting the Moscow region is situated to south and southwest from the Moscow region. Contrariwise the region wherefrom air masses with low aerosol upload come to the Moscow region is situated to west and northwest from the Moscow region (see Fig.1a).

For more reliable and accurate localization of the regions of potential sources of aerosol polluting the air in the Moscow region it is necessary: a) to extend datasets of local aerosol minima and local aerosol maxima and b) to localize the regions of potential sources of aerosols using similar clasterization of backward trajectories by other markers as Haenel parameter, presence/absence of sulphates, nitrates, organics in aerosols and so on.

For mapping the localizations in a wider space it is necessary: a) to calculate backward trajectories of air masses longer in time and space, b) to extend ensemble of backward trajectories and c) to extend aerosol datasets as well as to extend the number of parameters of aerosols to be analyzed including PM2.5-PM10, Haenel parameter, chemical composition and so on.

**References**

*1. Draxler, R.R. and Rolph, G.D., 2012. HYSPLIT (HYbrid Single-Particle Lagrangian Integrated Trajectory) Model access via NOAA ARL READY Website (http://ready.arl.noaa.gov/HYSPLIT.php). NOAA Air Resources Laboratory, Silver Spring, MD.*

*2. Rolph, G.D., 2012. Real-time Environmental Applications and Display sYstem (READY) Website (http://ready.arl.noaa.gov). NOAA Air Resources Laboratory, Silver Spring, MD.*

## Antarctic tropospheric temperature trends in reanalyses and radiosonde data

Ian Simmonds* and James A. Screen*,**

*School of Earth Sciences, The University of Melbourne, Victoria, 3010, Australia
** College of Engineering, Mathematics and Physical Sciences, University of Exeter, UK
simmonds@unimelb.edu.au

The Antarctic and subantarctic regions pose many problems for data collection, reanalyses and numerical modelling. The weather and climate in these domains are strongly influenced by complex topography, a range of atmosphere-ice-ocean interactions, intense inversions, strong baroclinicity, katabatic flow, etc. and, partly because of their remoteness, are poorly serviced by *in situ* observations. Many studies have made assessments of the quality of reanalysis products in the Antarctic region. For example, Bracegirdle et al. (2012) compared surface and radiosonde data from staffed Antarctic observation stations with output from five modern reanalyses for the period 1979-2008.

The radiosonde network in Antarctica provides a key data source for assessing analysis products and determining the nature of trends. A coherent Antarctic radiosonde network commenced in 1957-8, and the SCAR READER project (Turner et al. 2004) assembled these in convenient form and also undertook intensive (though basic) quality control of these records. More recently a number of groups have produced 'homogenised' sets of these observations which, in various ways, have accounted for changes in radiosonde type or observing practice over time. These sets include HadAT2 (Thorne et al. 2005), RICH-obs and RICH-tau (Haimberger et al. 2008), RAOBCORE (Haimberger et al. 2012), and IUK (Sherwood et al. 2008).

We have taken the seasonal **means** over these homogenised sets ('HOMOG'), and further averaged their 500hPa temperature over the eight available stations for the extended period 1961-2010 (other levels are considered in Screen and Simmonds (2012)). Fig. 1 shows these times series, and makes clear that their overall trends differ from those gleaned from the 1971–2003 period alone. The seasonal 1961-2010 temperature trends in both READER and HOMOG are all positive and all are significant with the exception of HOMOG in summer ($p = 0.12$).

*References*

Bracegirdle, T. J., and G. J. Marshall, 2012: The reliability of Antarctic tropospheric pressure and temperature in the latest global reanalyses. *J. Climate*, **25**, 7138-7146, doi: 10.1175/JCLI-D-11-00685.1.

Haimberger, L., et al., 2008: Toward elimination of the warm bias in historic radiosonde temperature records: Some new results from a comprehensive intercomparison of upper-air data. *J. Climate*, **21**, 4587-4606.

Haimberger, L., et al., 2012: Homogenization of the global radiosonde temperature dataset through combined comparison with reanalysis background series and neighboring stations. *J. Climate*, **25**, 8108-8131, doi: 10.1175/JCLI-D-11-00668.1.

Screen, J. A., and I. Simmonds, 2012: Half-century air temperature change above Antarctica: Observed trends and spatial reconstructions. *J. Geophys. Res.*, **117**, D16108, doi: 10.1029/2012JD017885.

Sherwood, S. C., et al., 2008: Robust tropospheric warming revealed by iteratively homogenized radiosonde data. *J. Climate*, **21**, 5336-5350.

Thorne, P. W., et al., 2005: Revisiting radiosonde upper air temperatures from 1958 to 2002. *J. Geophys. Res.*, **110**, D18105, doi: 10.1029/2004JD005753.

Turner, J., et al., 2004: The SCAR READER project: Toward a high-quality database of mean Antarctic meteorological observations. *J. Climate*, **17**, 2890-2898.

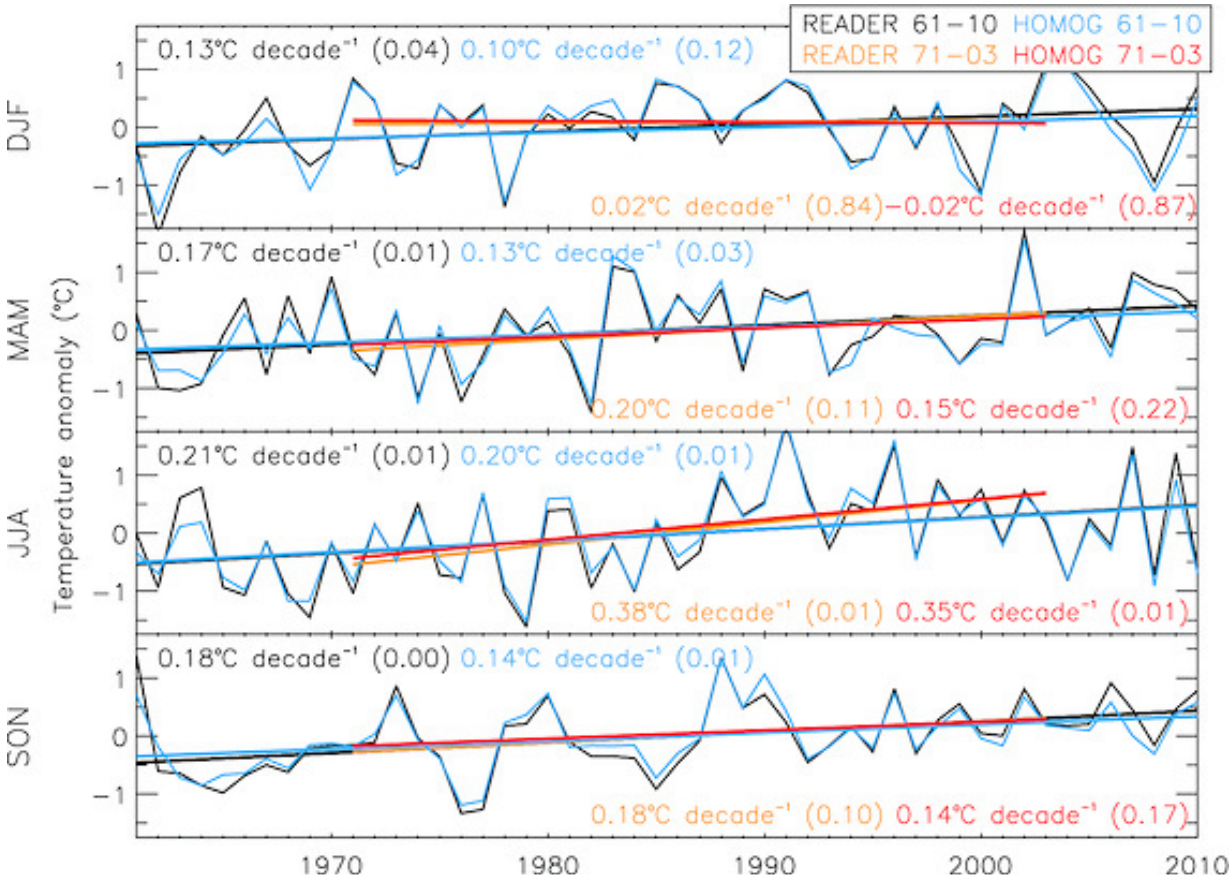


**Figure 1:** Seasonal multistation-mean 500 hPa temperature time series for READER (black) and HOMOG (blue). Also shown are the linear trends over two time periods, 1961–2010 and 1971–2003. The coloured numbers provide the regression slopes and their statistical significance ($p$; in parentheses).

# Investigation of a recent dramatic late-summer Arctic cyclone using the NCEP Climate Forecast System Reanalysis

Ian Simmonds and Irina Rudeva

School of Earth Sciences, The University of Melbourne, Victoria, 3010, Australia
simmonds@unimelb.edu.au

Our group is exploring the character of extreme storms in the Arctic basin. One focus of this work is to explore the role that surface processes may be playing in inducing these events, with especial attention on the influence of decreasing sea ice concentrations. (Previous work has shown there to be a close interaction between Arctic synoptic activity and sea ice (Simmonds et al. 2008, Simmonds and Keay 2009, Screen et al. 2011).) The analysis of the particular storm we undertake is performed with the NCEP Climate Forecast System Reanalysis (Saha et al. 2010) which is particularly suited to our approach because it has high in time and space resolution, and was executed in coupled mode involving the atmosphere, ocean, sea ice, and land.

The Arctic storm ('AS12') examined here was first identified by our objective cyclone tracking algorithm at 00UTC 2 August over Siberia before tracking east northeast, and crossing into the Arctic basin at 18UTC 4 August. AS12 subsequently made its way into the central Arctic and reached the minimum central pressure of 966.38 hPa at 18UTC 6 August. Figure 1 displays the CFSR MSLP at that time. The storm then travelled east and to the south and was last identified at 18UTC 14 August in the Canadian Arctic Archipelago, a lifetime of almost 13 days. The central pressure was also remarkable, it being the deepest August Arctic storm identified in the CFSR data set (which starts in 1979). AS12 was strongly influenced by a 300 hPa Tropopause Polar Vortex (see, e.g., Cavallo and Hakim (2012)) and strong tropospheric baroclinicity. Further details may be found in Simmonds and Rudeva (2012).

*References*

Cavallo, S. M., and G. J. Hakim, 2012: Radiative impact on tropopause polar vortices over the Arctic. *Mon. Wea. Rev.*, **140**, 1683-1702.

Saha, S., et al., 2010: The NCEP Climate Forecast System Reanalysis. *Bull. Amer. Meteor. Soc.*, **91**, 1015-1057.

Screen, J. A., et al., 2011: Dramatic interannual changes of perennial Arctic sea ice linked to abnormal summer storm activity. *J. Geophys. Res.*, **116**, D15105, doi:10.1029/2011JD015847.

Simmonds, I., and K. Keay, 2009: Extraordinary September Arctic sea ice reductions and their relationships with storm behavior over 1979-2008. *Geophys. Res. Lett.*, **39**, L19715, doi:10.1029/2009GL039810.

Simmonds, I., and I. Rudeva, 2012: The Great Arctic Cyclone of August 2012. *Geophys. Res. Lett.*, **39**, L23709, doi: 10.1029/2012GL054259.

Simmonds, I., et al., 2008: Arctic climate change as manifest in cyclone behavior. *J. Climate*, **21**, 5777-5796.

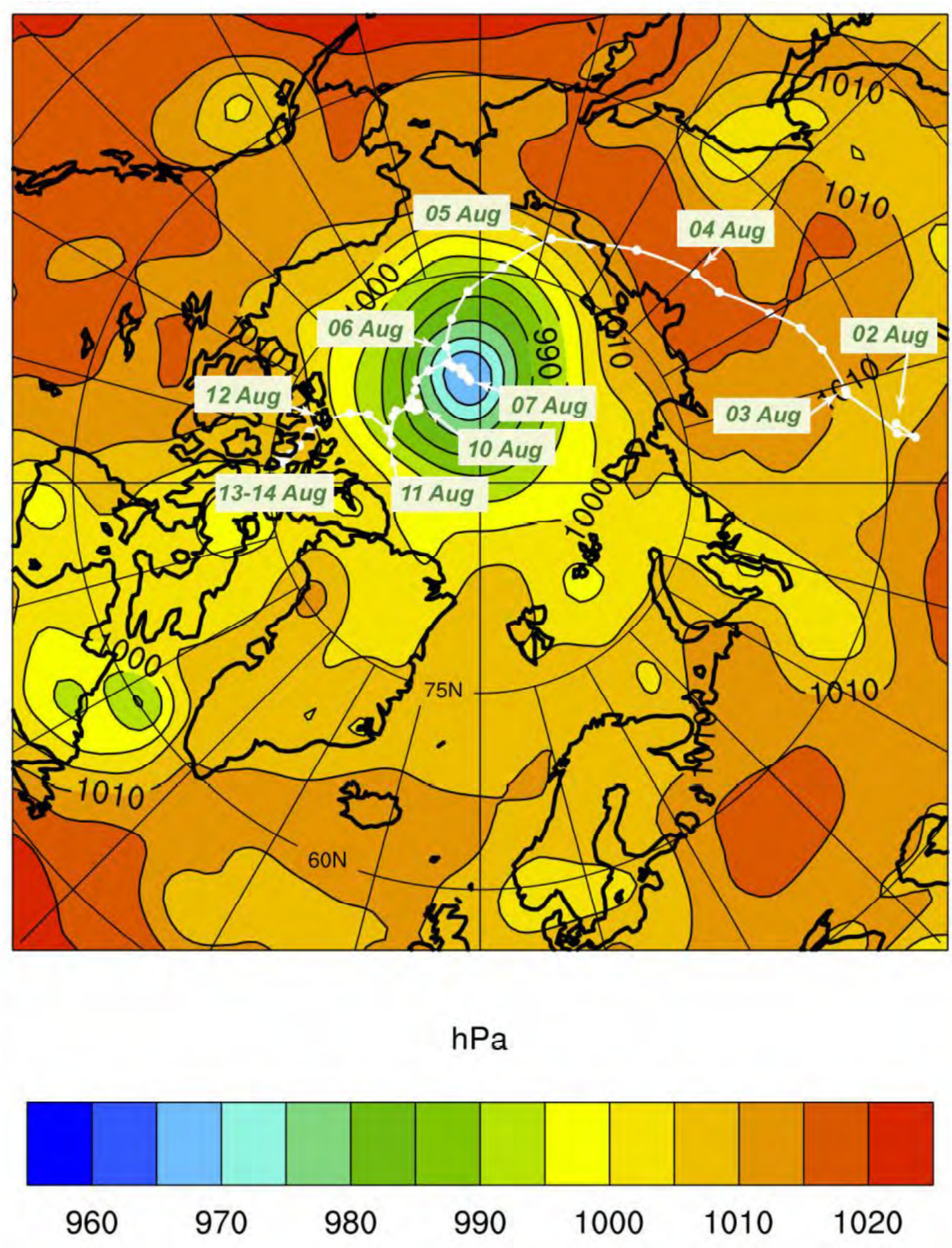


**Figure 1:** CFSR MSLP field (contour interval of 5 hPa) at 18UTC 6 August 2012, and the 6-hourly positions of AS12 from its formation to its demise.